RSC Advances

PAPER

View Article Online
View Journal | View Issue

Cite this: *RSC Adv.*, 2026, **16**, 16069

Conformational chirality in buckled molecular silicenes: a precursor for chiral magnets

Muskan,[a] Debojit Bhattacharya[b] and Suranjan Shil *[a]

Received 7th February 2026
Accepted 16th March 2026

DOI: 10.1039/d6ra01088a

rsc.li/rsc-advances

The chirality effect in bulk silicene has been studied under uniaxial tension, and Dirac Fermion chirality has also been observed in silicene on Ag (111). Despite these significant findings in bulk and surface-supported silicene, the existence and nature of chirality in molecular silicene, remain unknown. Herein, we report the "conformational chirality" in molecular silicene rings. This work also reports a computational study on silicene-based chiral magnetic systems that combines the structural flexibility of silicon with the spin functionality of organic radicals. Structural distortion introduces conformational chirality, making silicene an ideal platform for developing chiral magnetic materials. By coupling with silicene frameworks, organic nitronyl nitroxide (NN) radicals, a new class of diradicals are designed that exhibit both magnetism and chirality. These findings establish silicene-based chiral diradicals as promising candidates for applications in spintronics, quantum information science, and light-induced spin manipulation, setting the pathway for silicon-centered materials that describe chirality and magnetism.

1 Introduction

Chirality is a fundamental concept that plays a significant role in human life. It has tremendous importance in the chemical, pharmaceutical, and agricultural industries.[1] The origin of chirality in molecules and materials arises from different structural features, such as stereogenic centers, helicity, and symmetry breaking. In molecules, chirality commonly arises from (i) the presence of chiral stereocenters (*R*/*S* configurations), (ii) helical structures, and (iii) restricted symmetries that generate nonsuperimposable mirror images. Depending on the origin, these are termed stereogenic chirality, helical chirality, or axial chirality. For example, cumulenes exhibit axial chirality associated with helical molecular orbitals, whereas helicenes are classic examples of helical chirality.[2]

In recent years, chirality has gained importance from a technological viewpoint after the discovery of the chiral-induced spin selectivity (CISS) effect.[3,4] This effect demonstrates that electron spins can be preferentially filtered by chiral molecules, opening an entirely new field linking chirality with spintronics. Consequently, interest in the design and synthesis of chiral magnets and related systems to probe the origin of spin selectivity and explore their potential for future technologies has been increased.

Chiral magnets hold great promise for spin-optoelectronics because they can associate light and electron spins in new ways.[5,6] This connection makes it possible to control electron spins *via* circularly polarized light, helping to achieve low-power and contactless spin manipulation.[5,7,8] The breaking of spatial symmetry results in chirality, and broken time-reversal symmetry generates magnetism. However, determining exactly how chirality and magnetism work together is still a major scientific challenge.[7,9,10] Recently, researchers[11,12] have actively explored materials that combine chirality with ferromagnetism, hoping to create systems with enhanced magneto-optical effects.

Although chirality in bulk silicene has already been investigated by H. Zhao.[13] However, molecular silicene has not yet been synthesized, although several theoretical and computational studies are available.[14–18] The concept of silicene—a 2D silicon-based analog of graphene—was first coined by Guzman-Verri and Lew Yan Voon in 2007.[19] Silicene[19] is similar to graphene,[20] where a single layer of atomic Si is used as a building material. The experimental[21,22] and theoretical[17,18,23–25] studies of silicene are still limited. However, interest in silicene increased after Kara and colleagues successfully fabricated silicene nanoribbons on silver (Ag) surfaces,[21,26] expanding the landscape of two-dimensional materials beyond carbon-based systems.

Unlike graphene's perfectly flat structure, silicene's atoms form a slightly buckled, honeycomb pattern because silicon atoms are larger in size and can mix sp^2 and sp^3 hybridizations. Depending on its geometry and the presence of π electrons, silicon atoms in silicene can adopt either sp^2 or sp^3 hybridization. As a result, silicene rings such as hexasilicene prefer chair-like conformations because of this hybridization mixing.[27] In contrast, all the carbon atoms in polyacene rings are strictly sp^2

[a]*Manipal Centre for Natural Sciences, Manipal Academy of Higher Education, Manipal 576104, Karnataka, India. E-mail: suranjan.shil@manipal.edu; Tel: +91-820-2923580*
[b]*Kabi Sukanta High School (H.S.), Pati Colony, Siliguri, Darjeeling, West Bengal, 734010, India*

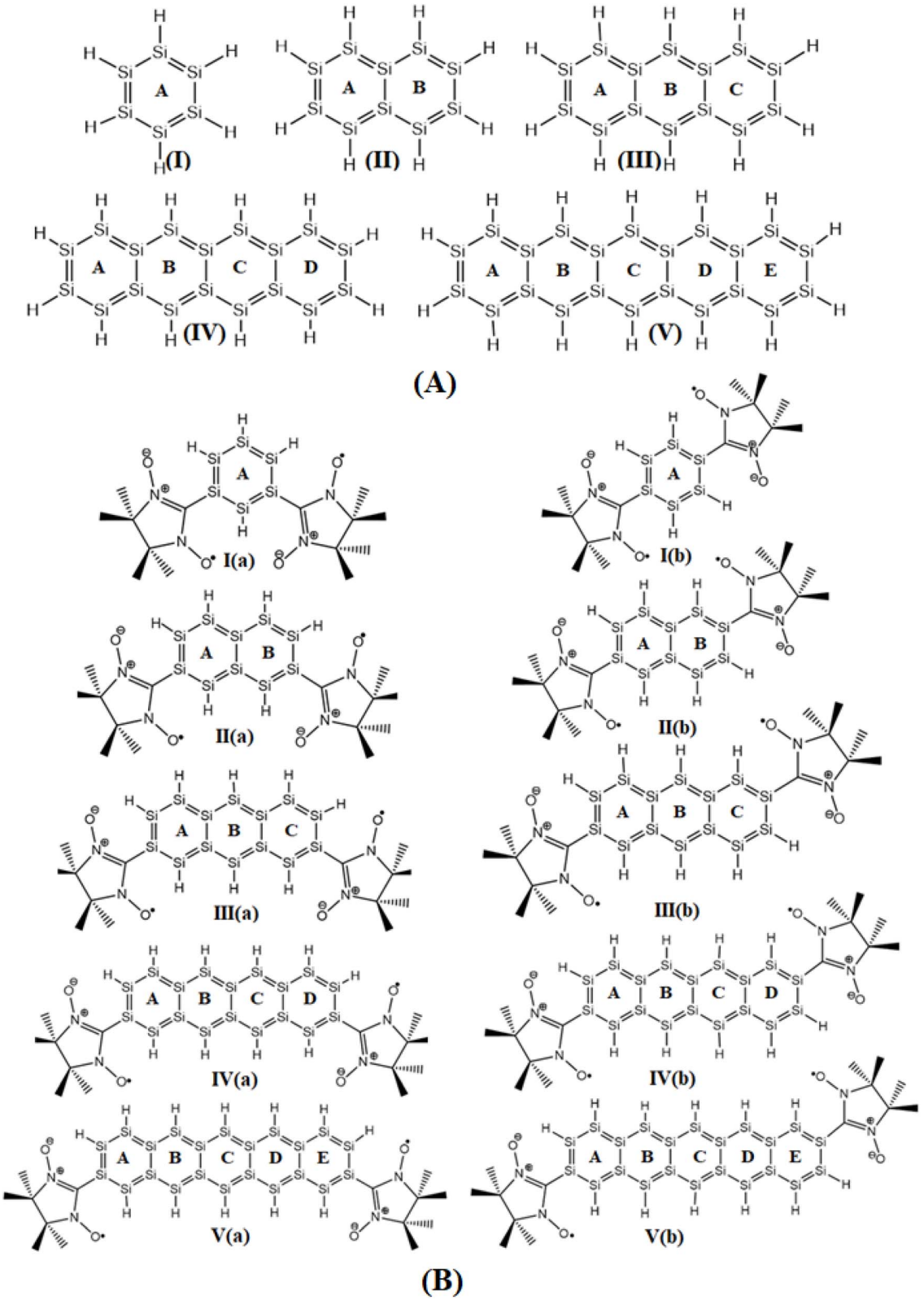

Fig. 1 (A) Silicene couplers from I–V. (B) Molecular structures of silicene-based diradicals I–V with bis NN radical units. [I(a)–V(a)] Odd atom connectivity [I(b)–V(b)] even atom connectivity along the silicene backbone. The rings are represented as A, B, C, D, and E for the coupler as well as for the diradicals for all the optimized molecules at the B3LYP/def2-TZVP level of theory.

hybridized, making those structures completely planar. This unique bonding flexibility allows silicene to form a variety of conformers, such as chair, boat, flat, and washboard shapes,[28] unlike the rigid planar geometry observed in purely carbon-based systems such as cyclohexane conformers.

In this work, we report that buckled six-membered silicene rings possess inherent conformational chirality due to their puckered geometry, which is similar to that of cyclohexane. Building on this chiral molecular silicene, we designed silicene-based diradical systems that retain chirality while introducing magnetic centers. The development of silicon-based chiral magnets thus represents a critical step toward integrating earth-abundant semiconductor elements with advanced spin functionalities, advancing the design of scalable, sustainable, and high-performance chiral electronic materials. These radical-based chiral magnets represent a new class of silicon-containing chiral molecules that could serve as promising candidates for future experimental studies on spin-selective transport and chiral molecular magnetism.

To understand how chirality and magnetism work together, we introduced diradicals that combine a semiconducting coupler, specifically, linear chiral silicene rings with organic bis-nitronyl nitroxide (NN) radicals. We computationally investigate a new class of molecular silicene-based diradicals, in which variable length mono to penta silicene units act as semiconducting couplers bridging bis-NN radicals. To explore the effects of the coupler topology on the magnetic and electronic properties, we constructed two distinct sets of diradicals (Fig. 1). In the first configuration (a) NN moieties are linked through an odd number of silicene atoms (odd connectivity), whereas the second configuration (b) is linked with an even number of silicene atoms (even connectivity) along the linear silicene framework.

2 Theoretical and computational details

Heisenberg, with his phenomenological spin Hamiltonian, expressed magnetic interaction between two magnetic sites as given in eqn (1):

$$\hat{H} = -2J\hat{S}_1\hat{S}_2 \quad (1)$$

where J, $\hat{S}_1$ and $\hat{S}_2$ denote the effective magnetic exchange coupling constant and the respective spin angular momentum operators. The coupling constant J is directly related to the energy difference between spin eigenstates and can be calculated as

$$E_{S=1} - E_{S=0} = -2J \quad (2)$$

Ferromagnetic interactions are found when J remains positive whereas negative sign of J, indicates antiferromagnetic interaction.

Multiconfigurational methods usually produce pure spin states without spin contamination; however, they are not commonly used as they are computationally expensive. Here, we used an alternative treatment that involves a broken symmetry formalism, which is less rigorous within the DFT framework. Note that computations in the DFT framework produce spin-contaminated wave functions. To remove the spin contamination, broken symmetry (BS) method was first proposed by Noodleman[29] Ginsberg[30] and Davidson[31] in the DFT framework for the weak overlap regime. Nonetheless, for the strong overlap regime, a formula is used by Bencini[32] and Ruiz.[33] However, despite being a strong and weak overlap regime for the moderate overlap regime (which is well designed for both the strong and weak overlap regimes), we use Yamaguchi's[34] widely applied formula, which is given below:

$$J_Y = \frac{(E_{BS} - E_T)}{\langle S^2\rangle_T - \langle S^2\rangle_{BS}} \quad (3)$$

Here, E_{BS} and E_T denotes the total energies of the broken-symmetry (BS) singlet and triplet states, respectively, whereas $\langle S^2\rangle_T$ and $\langle S^2\rangle_{BS}$ represent average spin-square values for triplet and BS states, respectively.

In the present study of silicene-based diradicals, multi-reference complete active space self-consistent field (CASSCF) approach have been performed using different active spaces for different diradicals to accurately predict the magnetic exchange coupling constant (J) according to the spin alternation rule on the DFT optimized geometry. As per the spin alternation rule the diradicals [I(a)–V(a)] should be ferromagnetically coupled whereas the diradicals [I(b)–V(b)] are antiferromagnetically coupled. The CASSCF method has been employed with the resolution of identity (RI) approximation to enhance computational efficiency, using the def2/JK auxiliary basis set for faster calculations. Since CASSCF wave functions are pure spin eigenstates, the value of $2J$ can be directly determined from the singlet and triplet energies using the following relation $2J = E_S - E_T$.

Nuclear-independent chemical shift (NICS[35]) values are calculated for each of the hexagonal rings of the silicene coupler and diradicals. The NICS values are calculated at the center of the ring, which is called NICS(0); however, as NICS(0) values are affected by the σ framework of Si–H and Si–Si bonds due to the perturbation of the π-cloud density by the σ network to obtain a more effective value of NICS, one must put the dummy atom at 1 Å above the π-ring system, which is the region above the π surface where the density of π-electrons is maximum and called NICS(1). NICS(1) is calculated above the plane defined by the four silicon atoms. Four Si atoms are in the plane out of the six Si atoms. The NICS has been calculated using the gauge-independent atomic orbital (GIAO)[36] methodology with the B3LYP functional and the def2-TZVP basis set with Gaussian16 software.[37]

Geometry-based aromatic quantitative index harmonic oscillator model of aromaticity (HOMA) is defined on the basis of changes in bond length. A higher aromaticity, indicated by a HOMA value closer to its higher ideal value of 1, and a lower value of nonaromatic conditions, indicated by a 0 value. Interestingly, it cannot be limited to the carbon framework; rather, HOMA indexing is far appreciated for its wide range of applicability.

The HOMA index was computed alongside the NICS to verify the consistency of the results. The HOMA values are calculated using the following formula.[38]

$$\mathrm{HOMA} = 1 - \frac{\propto}{n}\sum_{i=1}^{n}(R_0 - R_i)^2 \quad (4)$$

where α and R_0 are constants specific to Si–Si bonds in a hydrocarbon π system, n denotes the number of π bonds, R_i represents the observed or calculated length of the Si–Si bond within the ring, and summation is taken over all the π bonds. The HOMA values have been calculated using Multiwfn3.7 [39] based on the B3LYP/def2-TZVP optimized geometries.

To date, the optimal bond length (R_{opt}) and empirical constant alpha for Si–Si bonds have not been determined. We have calculated the values $\alpha = 101.6260$ and R_0 (Si–Si) = 2.225 Å *via* the following equation given by Krygowski[40] to calculate the HOMA indices.

$$R_{opt} = [R(s) + 2R(d)]/3 \quad (5)$$

$$\propto = 2([R(s) - R_{opt}]^2 + [R(d) - R_{opt}]^2)^{-1} \quad (6)$$

To calculate that, we took the single bond length of Si–Si as R(s) and the double bond length of Si=Si as R(d) as 2.3511 Å and 2.1629 Å, respectively, from the optimized geometry at the B3LYP/def2-TZVP level of theory.

A system must exhibit a significantly negative zero-field splitting (ZFS) parameter (D) to demonstrate single-molecule magnet (SMM) behavior. The ZFS parameters can be calculated using perturbative approaches within DFT,[41] where the spin–orbit coupling contributions are evaluated through unrestricted Kohn–Sham theory.[42,43] The axial (D) and rhombic (E) ZFS parameters are related to the anisotropy tensor components (Y_{xx}, Y_{yy}, Y_{zz}) as follows:

$$H_{ZFS} = D\left[S_z^2 - \frac{1}{3}S(S+1)\right] + E\left[S_x^2 - S_y^2\right] \quad (7)$$

where S denotes the total spin quantum number and $S_{x,y,z}$ denotes the spin matrices.

A negative D value indicates easy-axis anisotropy favorable for SMM behavior,[44] whereas a positive D value implies easy-plane anisotropy, which is not preferred for SMM.

The magnetic exchange coupling constants (J) for silicene-based nitronyl nitroxide diradicals are calculated with different DFT functionals, namely, GGA (*e.g.*, BP86, PBE), *meta*-GGA (*e.g.*, TPSS, M06L), global hybrid (B3LYP), hybrid M06 and range-separated hybrid (CAM-B3LYP) in two different configurations (a) and (b). A positive J value signifies ferromagnetic coupling, while a negative J indicates antiferromagnetic coupling, with the magnitude representing the coupling strength. All the molecular geometries have been fully optimized using the B3LYP functional paired with the def2-TZVP basis set, and J has been calculated employing multiple density functionals—B3LYP, BP86, TPSS, M06, M06-L, PBE, and CAM-B3LYP—to assess functional dependence comprehensively. Despite the spin contamination observed across all functionals, consistent results from the GGA functional PBE and the range-separated CAM-B3LYP functional led us to select PBE for all subsequent calculations, as it offers a balanced treatment while minimizing spin contamination. Circular dichroism (CD) spectra were evaluated *via* time-dependent DFT (TD-DFT) at the tight SCF PBE/def2-TZVP level for both the coupler and the full silicene-coupled diradical systems. All the calculations were performed using ORCA 6.0 software.[45]

The gauge-including magnetically induced current (GIMIC)[46,47] analysis has been performed using the GIMIC software, based on the formatted checkpoint file from the Gaussian program. The resulting current density maps and animations have been generated using the ParaView visualization tool.[48]

3 Results and discussion

3.1 Structural features and emergence of conformational chirality

Compared with graphene, silicene has a puckered or crinkled[49] structure and is less stable. Takahashi *et al.*[14] investigated polycyclic Si-hexagonal molecules *via* density functional theory (DFT) framework and reported that substituents having sp-hybrid orbitals with electron-donating ability increase the stability of the polycyclic structure. In $Si_{13}H_9$ to $Si_{60}H_{24}$, the H atoms at the edge of silicene are not flat but rather conformationally weakly buckled.[14] *Ab initio* calculations predicted a buckled honeycomb geometry for silicene, in contrast to the planar structure of graphene, despite their analogous electronic characteristics.[50,51] The buckling-induced symmetry breaking eliminates the instability of the high-symmetry planar configuration, an effect associated with the pseudo–Jahn–Teller (PJT) distortion.[52–54] Jose *et al.*[15] further carried out a σ–π separation analysis of Si_6H_6 and benzene as a function of the puckering angle, revealing that buckling stabilizes the σ-framework while destabilizing the π-framework. This distortion promotes σ–π mixing, leading to significant energetic stabilization of Si_6H_6, as supported by natural bond orbital (NBO) analysis.

We have calculated the silicon–silicon single- (2.351 Å) and double-bond (2.162 Å) lengths for H_3Si–SiH_3 and H_2Si–SiH_2 at the B3LYP/def2-TZVP level of theory. The calculated silicon–silicon bond lengths (2.20–2.29 Å) of all the molecules are given in Table 1 and lies between the Si–Si single and double bond lengths. The representation of all the bond length can be seen in Fig. 2(A). The silicon–silicon bond lengths are equal in hexasilabenzene (coupler I) owing to the onset puckering from $D_{6h} \rightarrow D_{3d}$ *via* b_{2g} distortion in hexasilabenzene.[15]

Jose *et al.*[55] reported that the stability of silicene clusters increases as the puckering angle becomes larger, which correlates with the increase in the number of rings from Si_6H_6 to $Si_{70}H_{22}$. The puckering angles ϕ (defined as the dihedral angles between atoms 1, 2, 3, 4, and 5 shown in Fig. 2(B)) calculated for all optimized geometries of silicene couplers at the B3LYP/def2-TZVP level of theory. The ϕ values for all the rings increase from coupler I to III; in the case of couplers IV and V, one of the ϕ values is lower than that of the previous smaller ring. One important point from the values of ϕ is that they are not equivalent to each other at the two ends of the silicene couplers

Table 1 The notation r_1–r_5 represents the bond length between the Si atoms shown in Fig. 2

Coupler	Bond length/Å
I	2.232/r_1
II	2.216/r_1, 2.260/r_2, 2.276/r_3, 2.249/r_4
III	2.256/r_1, 2.210/r_2, 2.268/r_3, 2.285/r_4, 2.245/r_5, 2.246/r_6
IV	2.259/r_1, 2.207/r_2, 2.270/r_3, 2.289/r_4, 2.239/r_5, 2.254/r_6, 2.291/r_7, 2.255/r_8, 2.240/r_9
V	2.261/r_1, 2.207/r_2, 2.272/r_3, 2.292/r_4, 2.237/r_5, 2.258/r_6, 2.294/r_7, 2.248/r_8

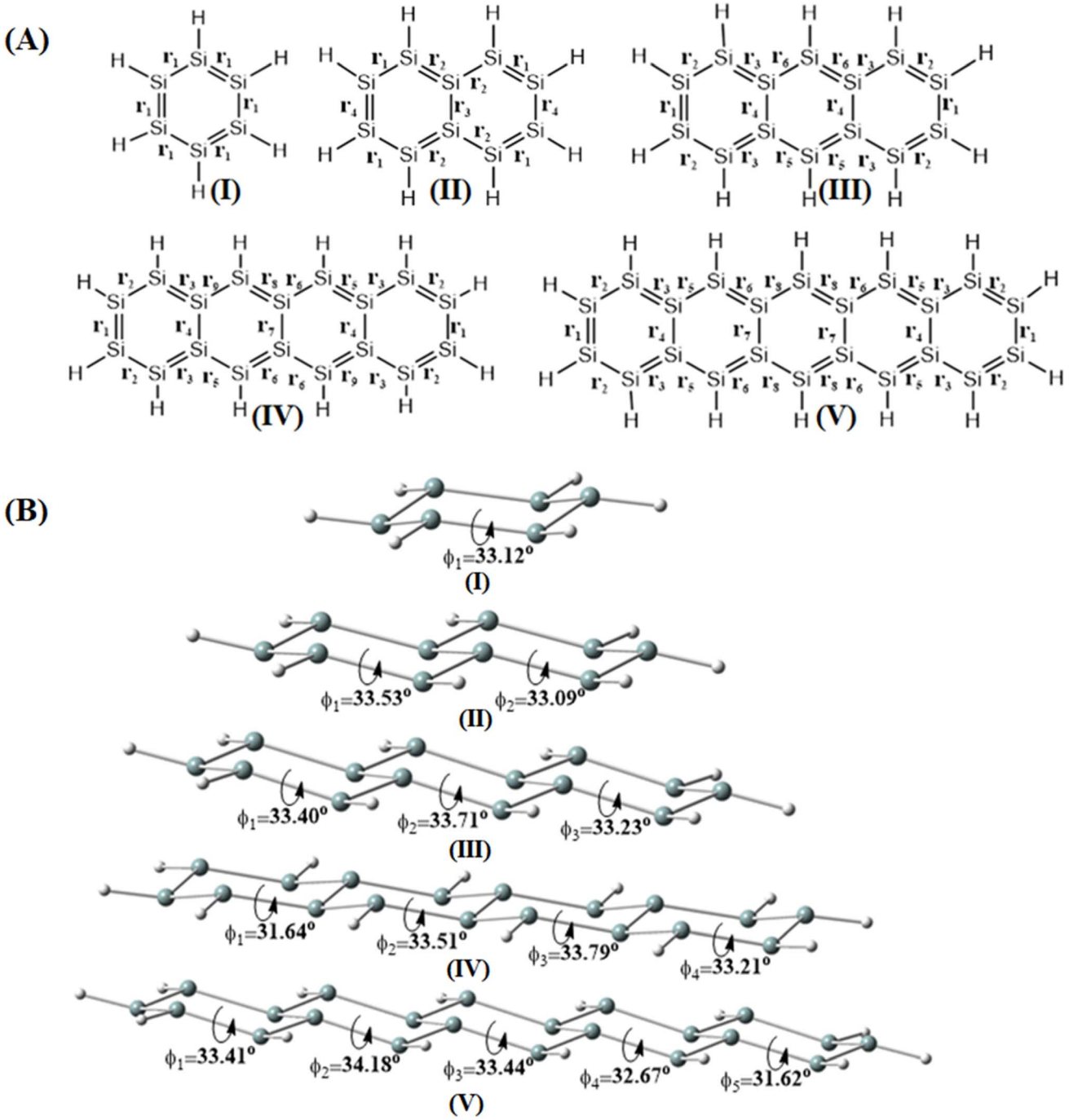

Fig. 2 (A) Silicene couplers from I–V. The notation r_1–r_5 represents the bond lengths between the adjacent Si atom at the B3LYP/def2-TZVP level of theory. (B) Representation of the puckering angle (ϕ_1, ϕ_2, ϕ_3, ϕ_4, ϕ_5) and their values of all the silicene couplers (I–V).

(where more than one ring is considered). For example, if we see the coupler V at one end, ϕ is 31.62°, and at the other end, it is 33.41°, which is true for all the couplers. The buckled structure of the silicenes can be attributed to the greater number of H-atoms at the end than in the center. Therefore, it is not possible to make a symmetric structure for these types of linear silicenes; hence, they show chiral behavior, which comes from their structural distortion. The chirality is discussed in the upcoming section.

3.2 Chiroptical response: simulated circular dichroism spectra

Circular dichroism (CD) spectroscopy[56] is used to detect chiral molecules through the absorption of circularly polarized light passing through them. It is commonly used to determine the chirality, absolute configuration, and structural features of molecules, as well as to study electronic transitions. Weerawardene *et al.*[57] studied polysiloacenes, which are silicon versions of acenes, *via* TDDFT calculations. The absorption spectra of these molecules showed three main peaks, called the α, β, and p bands, similar to those found in carbon acenes. These results indicate plasmon-like behavior in polysiloacenes, and as the number of fused rings increases, both the intensity and wavelength of the peaks also increase.

Fig. 3 shows the CD spectra of all the silicene couplers and the diradicals with their optical isomers in the range of 300–1200 nm. The oscillating pattern of the CD curves, with alternating positive and negative regions, indicates chiral electronic transitions and strong chiroptical activity. The blue and orange lines represent the CD spectra of the molecules and their mirror images. Differences in their CD spectra result from variations in the molecular environment, such as electronic interactions through the coupler or slight geometric distortions. The alternating signals suggest distinct chiral exciton coupling between the radical units, which is mediated by the coupler. As a result, all the molecules were confirmed to be chiral.

Notably, the chirality observed in these silicene-based diradicals arises purely from the puckered geometry, *i.e.*, only from silicene (here, a coupler), with no classical stereocenters present; hence, they are among rare examples of geometry-driven chiral radicals. Hence, we can call them "conformational chiral" molecules, or the phenomena called conformational chirality.

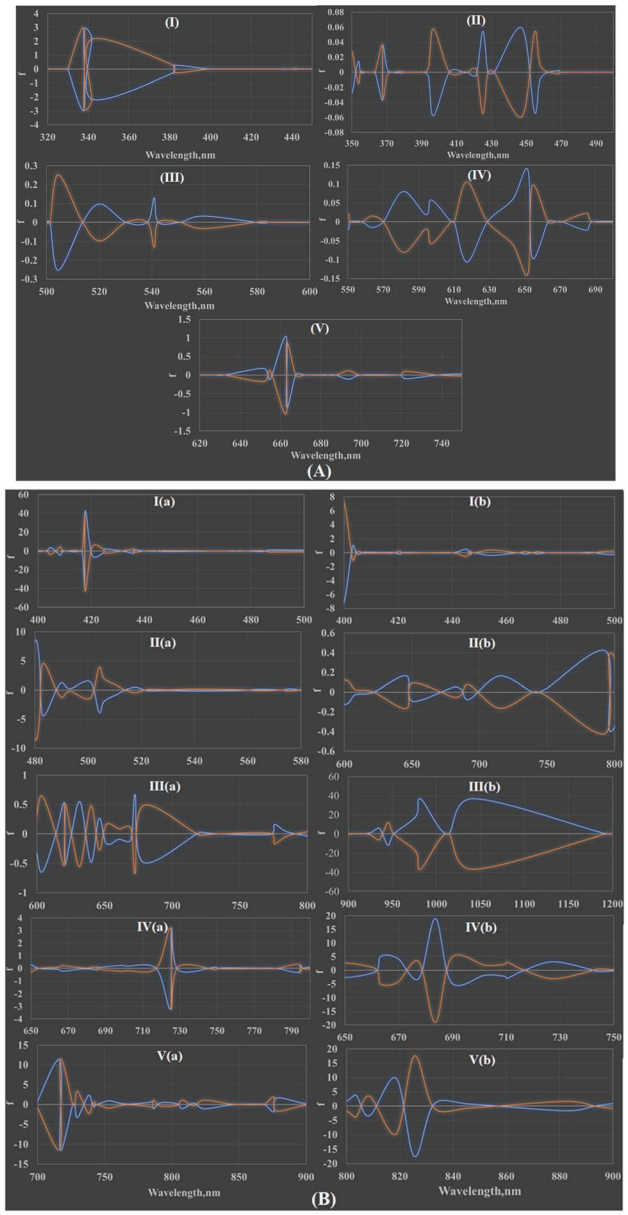

Fig. 3 (A) CD spectra of silicene couplers (I–V) without radicals. (B) CD spectra of the corresponding diradicals containing NN units in both configurations at the PBE/def2-TZVP level. The blue color represents the calculated CD spectra, whereas the orange color corresponds to their mirror images.

3.3 Aromaticity probed through NICS, HOMA, and GIMIC

We evaluated the aromatic characteristics of silicene couplers as well as diradicals *via* three complementary indices: nucleus-independent chemical shifts (NICS), harmonic oscillator model of aromaticity (HOMA), and gauge-including magnetically induced current (GIMIC).

The HOMA, NICS(0), and NICS(1) values are presented in Table 2 for all the silicene couplers as well as their corresponding diradicals. The HOMA values are close to 1 for all systems, indicating that the silicene rings are strongly aromatic in nature. The NICS(0) and NICS(1) values further support this conclusion, exhibiting consistent aromatic trends across the series. Notably, both the HOMA and NICS values slightly decrease with increasing ring size, indicating a slight decrease in aromatic character, which indicates the changes in electronic delocalization. Among the rings, the central (middle) ring displays relatively greater aromaticity, indicating greater delocalization within that specific region.

The NICS(0) values of all the coupler and diradicals are higher than those of NICS(1) (Table 2), which indicates that the σ aromaticity dominates over the π aromaticity.[58] This could be explained with the help of structure and orbital concepts. As the structure of the molecules is not completely planar, only four

Table 2 NICS and HOMA values of all the molecules. The ring notation can be seen in Fig. 1

Sl no.		Ring	A	B	C	D	E
I	Coupler	HOMA	0.99				
		NICS(0)	−11.01				
		NICS(1)	−9.88				
	(a)	HOMA	0.97				
		NICS(0)	−11.02				
		NICS(1)	−9.72				
	(b)	HOMA	0.98				
		NICS(0)	−11.34				
		NICS(1)	−10.04				
II	Coupler	HOMA	0.9	0.9			
		NICS(0)	−10.3	−10.29			
		NICS(1)	−9.66	−9.65			
	(a)	HOMA	0.9	0.9			
		NICS(0)	−10.14	−10.11			
		NICS(1)	−9.36	−9.25			
	(b)	HOMA	0.9	0.9			
		NICS(0)	−10.4	−10.38			
		NICS(1)	−9.55	−9.54			
III	Coupler	HOMA	0.85	0.85	0.85		
		NICS(0)	−9.81	−10.6	−9.81		
		NICS(1)	−9.16	−10.35	−9.16		
	(a)	HOMA	0.85	0.86	0.85		
		NICS(0)	−9.43	−9.86	−9.42		
		NICS(1)	−8.55	−9.6	−8.62		
	(b)	HOMA	0.9	0.93	0.86		
		NICS(0)	−9.89	−11.7	−10.42		
		NICS(1)	−9.02	−10.93	−9.47		
IV	Coupler	HOMA	0.83	0.82	0.82	0.83	
		NICS(0)	−9.33	−10.63	−10.63	−9.33	
		NICS(1)	−8.68	−10.38	−10.39	−8.67	
	(a)	HOMA	0.85	0.82	0.82	0.85	
		NICS(0)	−8.52	−8.33	−8.32	−8.48	
		NICS(1)	−7.53	−7.97	−7.95	−7.58	
	(b)	HOMA	0.83	0.82	0.83	0.84	
		NICS(0)	−9.33	−10.51	−10.54	−9.37	
		NICS(1)	−8.56	−10.26	−10.29	−8.52	
V	Coupler	HOMA	0.82	0.8	0.8	0.8	0.82
		NICS(0)	−8.97	−10.34	−11.06	−10.34	−8.95
		NICS(1)	−8.32	−10.11	−10.85	−10.14	−8.31
	(a)	HOMA	0.92	0.8	0.71	0.81	0.92
		NICS(0)	−9.59	−10.15	−10.1	−10.24	−9.63
		NICS(1)	−9.23	−10.27	−10.16	−10.18	−9.03
	(b)	HOMA	0.92	0.8	0.71	0.88	0.97
		NICS(0)	−9.06	−7.56	−5.73	−7.37	−9.24
		NICS(1)	−7.89	−6.89	−5.42	−7.15	−8.47

silicon atoms out of six atoms in a ring exist in one plane, which hinders π electron delocalization. The restricted delocalization of π electrons increases the electron density in the ring plane compared with that above or below the plane. This makes the silicene rings more σ aromatic (high NICS(0)) than π aromatic (low NICS(1)).

The calculated NICS(0)/(1) values of linear silicenes and silicene coupled diradicals follow the similar trend of polyacenes,[59] except in the case of diradical 5(b). In the middle ring, the highest aromatic condition arises, and hence, the flow of π-electrons from one side of the coupler to the other side is hindered. This is because the π-electrons from one end to the other end of the coupler need to cross a strongly aromatic environment.

Fliegl *et al.*[60] performed a detailed current density analysis for the model compound Si_6H_6 and recognized four distinct current pathways. One pathway involves a local atomic current that rotates around each of the six silicon atoms. The diatropic current encircling the center of the silicon ring, whereas two additional current pathways involve neighboring Si atoms; one forms an eight-shaped loop connecting Si and SiR groups—with a paratropic character at the SiR group and a diatropic character at the Si atom and another pathway runs diagonally across the Si_6 ring from one Si atom to another. These complex current patterns explain the unique ^{29}Si NMR chemical shift differences observed experimentally, although variations in bond order likely exert a stronger influence on these shifts than ring-current effects.[61]

The GIMIC plots for all the complexes are given in the SI (Fig. S1). The GIMIC analysis of silicene couplers (Panel A) and their corresponding diradicals (Panel B) shows similar current density patterns, validating the aromatic nature of the silicene framework. However, the radical-containing systems exhibit faster current flow, indicating enhanced electron delocalization and a stronger magnetic response. This accelerated current in diradicals arises from the coupling between the unpaired π-electrons and the conjugated silicene network, leading to a greater overall aromatic and spin-delocalized character.

The above discussions about aromaticity (NICS, HOMA, and GIMIC) indicate that the silicene rings are as aromatic as the benzenoid rings in polyacene.

3.4 Magnetic exchange coupling

The *J* values for all the complexes are given in Table 3 and detailed in the SI (Tables S3–S9) at different levels of theory, namely, B3LYP, BP86, M06, M06L, TPSS, CAM-B3LYP and PBE. For odd atom connectivity I(a)–V(a), *J* is positive, which means ferromagnetically coupled, with the exception of IV(a) in M06L and V(a) in BP86, TPSS, B3LYP and M06. For the even atom connectivity, I(b)–V(b) *J* is negative which signifies antiferromagnetic coupling. The PBE and CAM-B3LYP both give signs of *J*s representing both ferromagnetic and antiferromagnetic states and this follows the spin alternation rule, which means that the exchange coupling pathway through the coupler will follow even and odd numbers of bonds for the ferro- and antiferromagnetic paths, respectively.

All the functionals show spin contamination in producing S^2 values. Interestingly, the GGA functional PBE (Table S9 in the SI) produced more reliable spin-square (S^2) values than did the *meta*-GGA and hybrid functionals (Tables S3 and S5–S7 in the SI). These results showed that GGA functionals tend to provide a more proper description of the correct spin square values. In this work we rely on the PBE (GGA) functional for investigating the magnetic behavior of molecular systems with high diradical character.[62]

The *J* values of the diradicals decrease with increasing coupler length up to coupler III; however, they increase from couplers IV to V. Due to the increase in the radicaloid character

Table 3 Computed magnetic exchange coupling constants (J, cm^{-1} for silicene-based diradicals I–V using different density functionals (BP86, M06L, TPSS, B3LYP, M06, PBE, and CAM-B3LYP) and CASSCF. The values in parentheses represent $\langle S^2 \rangle$ expectation values for the high-spin and broken-symmetry low-spin states, respectively

Radicals		BP86	M06L	TPSS	B3LYP	M06	PBE	CAM-B3LYP	CASSCF
I	(a)	20.39 (2.03) (1.03)	49.42 (2.08) (1.06)	13.7 (2.05) (1.04)	79.09 (2.15) (1.11)	74.71 (2.14) (1.11)	22.54 (2.03) (1.02)	353.94 (2.49) (1.21)	0.52 (8e, 8o)
	(b)	−33.3 (2.03) (1.03)	−70.71 (2.05) (1.08)	−45.09 (2.04) (1.05)	−128.94 (2.11) (1.15)	−115.11 (2.10) (1.15)	−29.27 (2.02) (1.03)	−681.87 (2.20) (1.48)	−598.17 (8e, 8o)
II	(a)	12.28 (2.03) (1.03)	42.34 (2.10) (1.06)	20.77 (2.06) (1.05)	60.84 (2.17) (1.12)	31.85 (2.13) (1.12)	10.8 (2.03) (1.03)	456.88 (2.83) (1.25)	3.59 (6e, 6o)
	(b)	−15.02 (2.03) (1.03)	−54.58 (2.06) (1.10)	−27.23 (2.04) (1.06)	−85.91 (2.12) (1.17)	−83.16 (2.11) (1.17)	−15.87 (2.02) (1.03)	−1785.14 (2.24) (1.83)	−968.97 (8e, 8o)
III	(a)	12.02 (2.04) (1.03)	73.97 (2.21) (1.07)	24.72 (2.08) (1.05)	84.82 (2.27) (1.13)	97.33 (2.30) (1.13)	9.88 (2.04) (1.03)	744.16 (3.37) (1.37)	171.45 (6e, 6o)
	(b)	−12.52 (2.03) (1.04)	−2927.18 (3.06) (1.16)	−27.65 (2.05) (1.08)	−3254.26 (3.14) (1.24)	−3302.74 (3.14) (1.28)	−13.53 (2.03) (1.04)	−1186.31 (3.01) (2.28)	−327.20 (8e, 8o)
IV	(a)	25.67 (2.09) (1.03)	−1797.21 (3.10) (1.14)	63.11 (2.25) (1.06)	203.21 (2.65) (1.15)	239.72 (2.70) (1.15)	21.26 (2.07) (1.03)	1240.9 (3.94) (1.87)	10.56 (6e, 6o)
	(b)	−25.29 (2.03) (1.08)	−2150.9 (3.10) (1.54)	−1799.14 (3.03) (1.21)	−342.44 (2.33) (1.60)	−2595.95 (3.17) (1.67)	−1749.39 (2.96) (1.07)	−1223.93 (3.69) (2.90)	−145.04 (8e, 8o)
V	(a)	−874.44 (3.03) (1.51)	232.33 (3.07) (1.99)	−1025.05 (3.07) (1.75)	−1582.34 (3.19) (2.05)	−1721.06 (3.20) (2.11)	130.23 (2.55) (1.03)	784.86 (4.47) (3.28)	1341.82 (2e, 2o)
	(b)	−1022.01 (3.03) (1.60)	−1645.67 (3.12) (2.04)	−201.88 (2.73) (1.81)	−2065.54 (3.19) (2.15)	−2269.7 (3.19) (2.21)	−387.09 (2.03) (1.54)	−1169.62 (4.21) (3.42)	−741.60 (8e, 8o)

of the polyacene couplers, the J values increase with increasing coupler length,[59] similar trend of J values observed in this work. This is due to the generation of radicaloid character in higher silicene, as tabulated in the SI (Table S2). However, the magnitude of the J value is greater for silicene-coupled diradicals compared to the polyacene based diradicals. Therefore, we can say that much higher itinerant exchange has occurred through silicene spacers. This result signifies that the silicenes behave similarly like polyacenes with respect to the calculated J values. To validate the values of DFT calculated magnetic exchange coupling constant we have also employed the CASSCF method to evaluate the J values (Table 3).

3.5 Frontier molecular orbitals

The molecular orbital plots of all the silicene-based diradicals are shown in Fig. S2 (SI).

From the plots, it can be observed that in the SOMOs, the orbitals are mainly localized on the radical sites, whereas in the LUMOs, they are more localized on the silicene coupler. The SOMO–SOMO energy gap remains nearly constant across the series, whereas the HOMO–LUMO gap gradually decreases as the number of silicene rings increases. We have found that the highest J values produced by the diradical where the HOMO–LUMO gap is lowest for the ferromagnetic diradicals (Fig. S3).

3.6 Electron delocalization and spin density analysis

The spin density distribution analysis for these silicene-based diradicals provides insight about the magnetic interactions between the radical centers. The spin alternation rule[63,64] states that in conjugated systems, the spin density alternates in sign (positive and negative) across adjacent atoms or groups. This phenomenon arises from the delocalized nature of the unpaired electron within the molecular framework. This alternation ensures stabilization of the radical system *via* resonance and spin delocalization. If the diradical is connected *via* odd number of atoms with π orbitals, then the diradical will behave as a ferromagnet, and for even number of atoms, the diradical will behave as an antiferromagnet.

Spin density plots can be seen in Fig. 4. The spin population for both configurations first decreases from diradical (I to III) and increasing from (IV to V), and one can also see the same pattern in J values (PBE).

3.7 Zero-field splitting

The zero-field splitting (ZFS) parameter is essential for evaluating the potential of high-spin molecular systems as single-molecule magnet. In this work, ZFS values have been calculated for all the ferromagnetically coupled diradical complexes (Table S1 in SI).

All the ferromagnetically coupled diradicals have negative D values and small E/D values. This makes these complexes strong candidates for use as single-molecule magnets. The diradical I(a) has the highest negative D and low E/D values. This makes diradical I(a) the most promising candidate for single-molecule magnets among all the diradicals studied here. The diradical V(a) has the highest J value with the highest E/D value, which

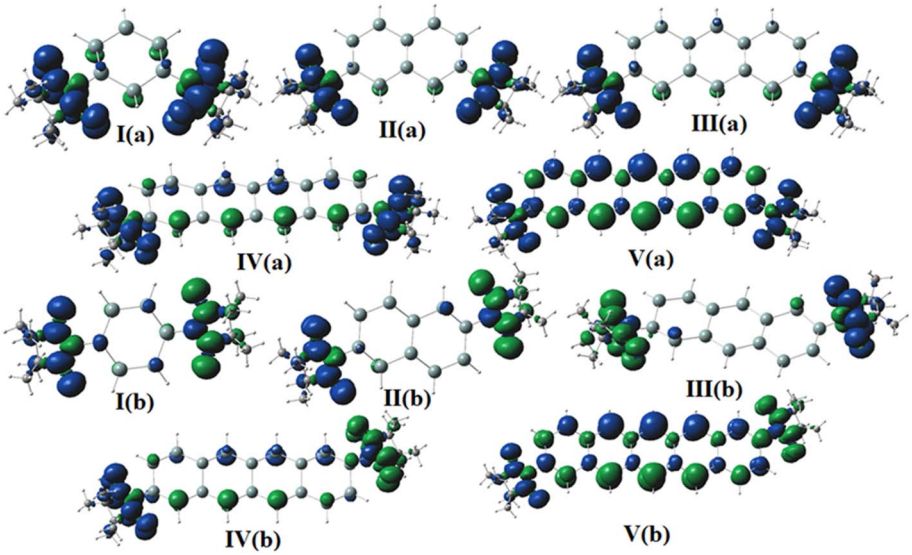

Fig. 4 Spin density distributions of silicene-based diradicals (I–V) computed at the PBE/def2-TZVP level. Panels (a) show the high-spin triplet states, whereas panels (b) correspond to the broken-symmetry (BS) states. The blue and green lobes represent α- and β-spin densities, respectively, highlighting the localization and delocalization of unpaired electrons across the silicene couplers and nitronyl nitroxide radical centers. The iso value is 0.001.

makes it the least possible single-molecule magnet among all the diradicals.

4 Conclusion

The molecular silicene shows conformational chirality due to the buckling of the ring. The chirality of the silicene has been confirmed from the computed CD spectra. The aromaticity indices, such as NICS, HOMA and GIMIC, indicate that linear silicene shows aromatic behavior similar to that of linear polyacene. The NICS(0), *i.e.*, the σ aromaticity of these silicenes, is stronger than the π aromaticity (NICS(1)). This behavior of the linear silicenes is due to the restricted delocalization of π electrons in the ring plane compared with those above or below the plane. The magnetic behavior of the silicene-coupled diradicals makes them potential candidate for a single-molecule magnet, which is confirmed from the zero-field splitting parameter (D) and E/D values. The trend of magnetic exchange coupling constant values of silicene-coupled diradicals resembles that of polyacene-coupled diradicals. These results confirm that linear molecular silicene shows similar behavior to that of polyacene with fascinating chiral behavior. This work could lead to the opening of a new area in the fields of chiral molecules and chiral magnets and could lead experimentalists in their synthesis.

Conflicts of interest

There are no conflicts to declare.

Data availability

The data supporting this article have been included as part of the supplementary information (SI). Supplementary information: the GIMIC plot, molecular orbitals, ZFS values, diradical character, energies of both the conformers, HOMO–LUMO *vs.* J plot, energy and spin square values with different functionals and optimized coordinates of all the molecules are available. See DOI: https://doi.org/10.1039/d6ra01088a.

Acknowledgements

Manipal Centre for Natural Sciences, Centre of Excellence, Manipal Academy of Higher Education (MAHE) is acknowledged for providing the facilities and support. Muskan acknowledges the TMA Pai Fellowship provided by MAHE. SERB India is acknowledged for financial support *via* grant no. SRG/2022/000822. This research work has used the high computing facility Paramutkarsh, CDAC, Bangalore.

References

1 L. A. Nguyen, H. He and C. Pham-Huy, *Int. J. Biomed. Sci.*, 2006, **2**, 85–100.
2 M. H. Garner, A. Jensen, L. O. H. Hyllested and G. C. Solomon, *Chem. Sci.*, 2019, **10**, 4598–4608.
3 R. Naaman, Y. Paltiel and D. H. Waldeck, *Nat. Rev. Chem.*, 2019, **3**, 250–260.
4 K. Ray, S. P. Ananthavel, D. H. Waldeck and R. Naaman, *Science*, 1999, **283**, 814–816.
5 Z. Wang and W. Qin, *NPG Asia Mater.*, 2021, **13**, 17.
6 Z. Li, Q. Fan, Z. Ye, C. Wu, Z. Wang and Y. Yin, *Science*, 2023, **380**, 1384–1390.
7 H. Bauke, S. Ahrens and R. Grobe, *Phys. Rev. A*, 2014, **90**, 052101.

8 A. J. Landig, J. V. Koski, P. Scarlino, U. C. Mendes, A. Blais, C. Reichl, W. Wegscheider, A. Wallraff, K. Ensslin and T. Ihn, *Nature*, 2018, **560**, 179–184.
9 R. Erhard and H. Bauke, *Phys. Rev. A*, 2015, **92**, 042123.
10 M. M. Dellweg and C. Müller, *Phys. Rev. A*, 2017, **95**, 042124.
11 Z. Wang, M. Gao, M. Wei, S. Ren, X.-T. Hao and W. Qin, *ACS Nano*, 2019, **13**, 4705–4711.
12 L. D. Barron, *Nat. Mater.*, 2008, **7**, 691–692.
13 H. Zhao, *Phys. Lett. A*, 2012, **376**, 3546–3550.
14 M. Takahashi, *Sci. Rep.*, 2017, **7**, 10855.
15 D. Jose and A. Datta, *J. Phys. Chem. C*, 2012, **116**, 24639–24648.
16 D. Jose and A. Datta, *Acc. Chem. Res.*, 2014, **47**, 593–602.
17 K. Takeda and K. Shiraishi, *Phys. Rev. B: Condens. Matter Mater. Phys.*, 1989, **39**, 11028–11037.
18 K. Takeda and K. Shiraishi, *Phys. Rev. B: Condens. Matter Mater. Phys.*, 1994, **50**, 14916–14922.
19 G. G. Guzmán-Verri and L. C. Lew Yan Voon, *Phys. Rev. B: Condens. Matter Mater. Phys.*, 2007, **76**, 075131.
20 K. S. Novoselov, A. K. Geim, S. V. Morozov, D. Jiang, Y. Zhang, S. V. Dubonos, I. V. Grigorieva and A. A. Firsov, *Science*, 2004, **306**, 666–669.
21 H. Nakano, M. Ishii and H. Nakamura, *Chem. Commun.*, 2005, 2945.
22 H. Nakano, T. Mitsuoka, M. Harada, K. Horibuchi, H. Nozaki, N. Takahashi, T. Nonaka, Y. Seno and H. Nakamura, *Angew. Chem.*, 2006, **118**, 6451–6454.
23 Y. Wang, K. Scheerschmidt and U. Gösele, *Phys. Rev. B: Condens. Matter Mater. Phys.*, 2000, **61**, 12864–12870.
24 X. Yang and J. Ni, *Phys. Rev. B: Condens. Matter Mater. Phys.*, 2005, **72**, 195426.
25 E. Durgun, S. Tongay and S. Ciraci, *Phys. Rev. B: Condens. Matter Mater. Phys.*, 2005, **72**, 075420.
26 A. Kara, C. Léandri, M. E. Dávila, P. De Padova, B. Ealet, H. Oughaddou, B. Aufray and G. Le Lay, *J. Supercond. Nov. Magn.*, 2009, **22**, 259–263.
27 A. Molle, C. Grazianetti, L. Tao, D. Taneja, Md. H. Alam and D. Akinwande, *Chem. Soc. Rev.*, 2018, **47**, 6370–6387.
28 S. Balendhran, S. Walia, H. Nili, S. Sriram and M. Bhaskaran, *Small*, 2015, **11**, 640–652.
29 L. Noodleman, *J. Chem. Phys.*, 1981, **74**, 5737–5743.
30 A. P. Ginsberg, *J. Am. Chem. Soc.*, 1980, **102**, 111–117.
31 L. Noodleman and E. R. Davidson, *Chem. Phys.*, 1986, **109**, 131–143.
32 A. Bencini and D. Gatteschi, *J. Am. Chem. Soc.*, 1986, **108**, 5763–5771.
33 E. Ruiz, J. Cano, S. Alvarez and P. Alemany, *J. Comput. Chem.*, 1999, **20**, 1391–1400.
34 K. Yamaguchi, Y. Takahara, T. Fueno and K. Nasu, *Jpn. J. Appl. Phys.*, 1987, **26**, L1362.
35 Z. Chen, C. S. Wannere, C. Corminboeuf, R. Puchta, P. Von and R. Schleyer, *Chem. Rev.*, 2005, **105**, 3842–3888.
36 K. Wolinski, J. F. Hinton and P. Pulay, *J. Am. Chem. Soc.*, 1990, **112**, 8251–8260.
37 M. J. Frisch, G. W. Trucks, H. B. Schlegel, G. E. Scuseria, M. A. Robb, J. R. Cheeseman, G. Scalmani, V. Barone, G. A. Petersson, H. Nakatsuji, X. Li, M. Caricato, A. V. Marenich, J. Bloino, B. G. Janesko, R. Gomperts, B. Mennucci, H. P. Hratchian, J. V. Ortiz, A. F. Izmaylov, J. L. Sonnenberg, D. Williams-Young, F. Ding, F. Lipparini, F. Egidi, J. Goings, B. Peng, A. Petrone, T. Henderson, D. Ranasinghe, V. G. Zakrzewski, J. Gao, N. Rega, G. Zheng, W. Liang, M. Hada, M. Ehara, K. Toyota, R. Fukuda, J. Hasegawa, M. Ishida, T. Nakajima, Y. Honda, O. Kitao, H. Nakai, T. Vreven, K. Throssell, J. A. Montgomery Jr, J. E. Peralta, F. Ogliaro, M. J. Bearpark, J. J. Heyd, E. N. Brothers, K. N. Kudin, V. N. Staroverov, T. A. Keith, R. Kobayashi, J. Normand, K. Raghavachari, A. P. Rendell, J. C. Burant, S. S. Iyengar, J. Tomasi, M. Cossi, J. M. Millam, M. Klene, C. Adamo, R. Cammi, J. W. Ochterski, R. L. Martin, K. Morokuma, O. Farkas, J. B. Foresman and D. J. Fox, *Gaussian 16, Revision C.01*, Gaussian, Inc., Wallingford CT, 2019.
38 J. Kruszewski and T. M. Krygowski, *Tetrahedron Lett.*, 1972, **13**, 3839–3842.
39 T. Lu and F. Chen, *J. Comput. Chem.*, 2012, **33**, 580–592.
40 T. M. Krygowski, *J. Chem. Inf. Comput. Sci.*, 1993, **33**, 70–78.
41 P. J. Desrochers, J. Telser, S. A. Zvyagin, A. Ozarowski, J. Krzystek and D. A. Vicic, *Inorg. Chem.*, 2006, **45**, 8930–8941.
42 S. Zein, C. Duboc, W. Lubitz and F. Neese, *Inorg. Chem.*, 2008, **47**, 134–142.
43 F. Neese, *J. Chem. Phys.*, 2007, **127**, 164112.
44 F. Neese and D. A. Pantazis, *Faraday Discuss.*, 2011, **148**, 229–238.
45 F. Neese, *Wiley Interdiscip. Rev.: Comput. Mol. Sci.*, 2022, **12**, e1606.
46 S. Taubert, D. Sundholm and J. Jusélius, *J. Chem. Phys.*, 2011, **134**, 054123.
47 J. Jusélius, D. Sundholm and J. Gauss, *J. Chem. Phys.*, 2004, **121**, 3952–3963.
48 J. Ahrens, B. Geveci and C. Law, *Visualization Handbook*, 2005, pp. 717–731.
49 G. Brumfiel, *Nature*, 2013, **495**, 152–153.
50 G. G. Guzmán-Verri and L. C. Lew Yan Voon, *Phys. Rev. B: Condens. Matter Mater. Phys.*, 2007, **76**, 075131.
51 H. Şahin, S. Cahangirov, M. Topsakal, E. Bekaroglu, E. Akturk, R. T. Senger and S. Ciraci, *Phys. Rev. B: Condens. Matter Mater. Phys.*, 2009, **80**, 155453.
52 R. Pushpa, S. Narasimhan and U. Waghmare, *J. Chem. Phys.*, 2004, **121**, 5211–5220.
53 L. Blancafort, M. J. Bearpark and M. A. Robb, *Mol. Phys.*, 2006, **104**, 2007–2010.
54 W. D. Hobey, *J. Chem. Phys.*, 1965, **43**, 2187–2199.
55 D. Jose and A. Datta, *Phys. Chem. Chem. Phys.*, 2011, **13**, 7304.
56 B. Komjáti, Á. Urai, S. Hosztafi, J. Kökösi, B. Kováts, J. Nagy and P. Horváth, *Spectrochim. Acta, Part A*, 2016, **155**, 95–102.
57 K. L. D. M. Weerawardene and C. M. Aikens, *J. Phys. Chem. Lett.*, 2015, **6**, 3341–3345.
58 S. Paul and A. Misra, *Inorg. Chem.*, 2011, **50**, 3234–3246.
59 D. Bhattacharya, S. Shil, A. Misra and D. J. Klein, *Theor. Chem. Acc.*, 2010, **127**, 57–67.
60 H. Fliegl, S. Taubert, O. Lehtonen and D. Sundholm, *Phys. Chem. Chem. Phys.*, 2011, **13**, 20500.

61 R. J. F. Berger, H. S. Rzepa and D. Scheschkewitz, *Angew. Chem., Int. Ed.*, 2010, **49**, 10006–10009.
62 C. Debbarma, D. Bhattacharya and S. Shil, *J. Comput. Chem.*, 2025, **46**, e70230.
63 A. A. Ovchinnikov LYa Karpov, *Theor. Chim. Acta*, 1978, **47**, 297–304.
64 C. Trindle and S. N. Datta, *Int. J. Quantum Chem.*, 1996, **57**, 781–799.